Saturated patterned excitation microscopy with two-dimensional excitation patterns

Rainer Heintzmann*

Max-Planck Institute for Biophysical Chemistry, Am Fassberg 11, Göttingen 37077, Germany

Abstract

The techniques of patterned excitation microscopy (PEM, also referred to in the literature as structured illumination, harmonic excitation light microscopy, or laterally modulated excitation microscopy), has recently been extended to the non-linear regime, permitting a further increase in resolution breaking the Abbe diffraction limit (saturated PEM, saturated patterned excitation microscopy (SPEM)). Fluorescence saturation was suggested as the non-linear effect employed to achieve this aim. Here a two-dimensional extension of the linear and the non-linear patterned excitation technique is introduced and simulations of the expected resolution improvement are presented. The simulations account for photon statistics, a sub-optimal degree of modulation and a high amount of background fluorescence in the sample. The resulting point-spread-functions achieve a full width at half maximum of 215 nm (widefield), 118 nm (linear PEM), and 57 nm (saturated PEM, 9×9 orders). For higher resolution, an increased number of detected photons and of raw data images are required. A potential method for substantially decreasing the required number of raw images in PEM and SPEM is discussed.
© 2003 Elsevier Ltd. All rights reserved.

Keywords: Structured illumination; Non-linear microscopy; Resolution enhancement; Widefield; Virtual microscopy

1. Introduction

In a recent publication (Heintzmann et al., 2002) the concept of saturated patterned excitation microscopy (SPEM) was introduced. This method is a non-linear extension of various linear techniques (in this article referred to as patterned excitation microscopy, PEM), laterally modulated excitation microscopy (LMEM) (Heintzmann and Cremer, 1999), structured illumination microscopy (Gustafsson, 2000; Gustafsson et al., 2000) and harmonic excitation light microscopy HELM (Frohn et al., 2000, 2001). All of these methods are based on the separation of overlapping components of the imaged object in Fourier-space. As an effect of patterned excitation, these components are shifted in Fourier-space in relation to each other. Therefore, each separated component can be reassigned to its 'native' places, such that the zero frequency of each component corresponds to the zero frequency in Fourier-space, resulting in an improved resolution since an enlarged region of sample information in reciprocal space has been transferred in comparison to flat illumination widefield microscopy.

The non-linear extension of PEM by use of fluorescence saturation introduces further such components at even higher spatial frequencies, which can again be separated and reassembled, enhancing the range of transferable spatial frequencies and thus the resolution (Heintzmann et al., 2002). As with other non-linear microscopy methods (Schönle et al., 1999; Klar et al., 2000) the diffraction barrier (Abbe Limit) can then be overcome.

The aim of this article is to expand the method of patterned excitation to two-dimensional excitation patterns, and to expand the treatment of how to optimally reassemble the extracted object components.

2. Methods

In this section, the steps of data-processing along with the theory will be described in detail in the order in which they are computed in the simulation. It will start with a description of the patterns, followed by the effect of fluorescence saturation, image formation and finally

---

* Tel.: +49-551-201-1029; fax: +49-551-201-1467.
E-mail address: rheintz@gwdg.de (R. Heintzmann).

the image reconstruction, in which the structure of the excitation pattern is determined from the noisy data and the final result is obtained by a weighted averaging procedure in Fourier space.

The simulations presented below were all carried out on a grid (162×162 pixels) with 15 nm sampling distance. The point spread function (PSF) for imaging was simulated using high numerical aperture vector theory (Egner and Hell, 1999) at a wavelength of 520 nm, aplanar apodization, a numerical aperture of 1.3 and a refractive index of 1.518. These parameters yielded a widefield cut-off frequency at a relative distance (relative frequency) of 15% to the Fourier-transformed image border (in X or Y).

The distance of the illuminating dots, arranged in a two-dimensional square grid, were 27 pixels (405 nm in object space) in X and Y. The first-order diffraction spots from coherent illumination (at 488 nm) of this dot pattern would hit the back focal plane of the objective at 92.7% of the acceptance radius.

Photon noise was introduced into the images according to a Poissonian distribution. 10^4 expected photons were assumed in the brightest pixel.

Most parameters (the PSF, the sampling and the relative saturation) of these simulations corresponded closely to a previous publication (Heintzmann et al., 2002).

2.1. Two-dimensional patterns for excitation

A possible setup for generating two-dimensional excitation patterns that can be altered/shifted reliably along two dimensions, is shown in Fig. 1. The pattern is generated by illumination of a spatial light modulator (SLM), displaying a periodic structure with coherent light. To further influence the pattern and enhance its modulation depth, an order-selection aperture can be introduced, which can suppress certain diffraction orders and transmit others. Fig. 2 displays the simulated excitation patterns. Panel (a) shows the simulated excitation pattern in the sample plane originating from a point grid under normal illumination with coherent light. The parameters have been selected such that only four first diffraction orders and the zero diffraction order pass
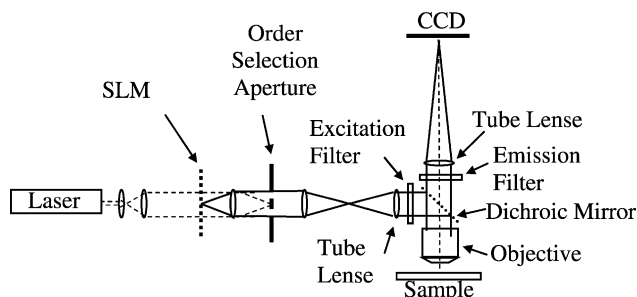

Fig. 1. Possible experimental setup for two-dimensional patterned excitation. In the case of saturated patterned excitation microscopy (SPEM) the light source (here laser) needs to be strong enough to cause a non-linear dependence of the emitted light intensity on the local illumination intensity.
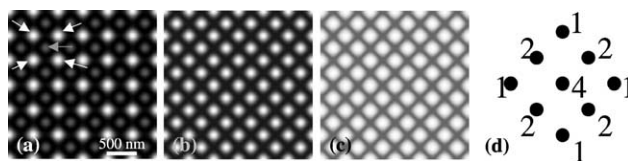

Fig. 2. The excitation pattern in real space. (a) Simulated intensity pattern $I_{ex}(x,y)$ in the object plane generated assuming a square grid and passing the zero and the first diffracted orders through the back aperture. The grey arrow marks a 'ghost' spot stemming from the coherent illumination (neglecting polarization effects). (b) Illumination pattern when the zero diffraction order is removed from the illumination. (c) The emittability pattern resulting from (b) at high intensities. 10% background intensity were assured prior to the influence of saturation. This pattern was used in the SPEM simulations. (d) Schematic representation of the illumination pattern (b) in Fourier-space. The numbers indicate the relative strength of the orders.

through the back aperture of the objective. In other words, the excitation pattern is generated by the interference of five planar waves. Furthermore, a scalar theory was assumed for the illumination part, not considering the polarization effects. The two dimensional excitation intensity pattern $I_{ex}(x,y)$ in the plane of focus can be described as

$$A_{ex}(x,y) = \exp(ik(x - \Delta x)) + \exp(-ik(x - \Delta x))$$
$$+ \exp(ik(y - \Delta y)) + \exp(-ik(y - \Delta y)) + m \quad (1)$$

$$I_{ex}(x,y) = |A_{ex}(x,y)|^2 = A_{ex}(x,y)A_{ex}^*(x,y)$$

The star ($*$) stands for the complex conjugate and $i := \sqrt{-1}$. The complex-valued amplitude function is the sum of plane waves (here in 2D) without loss of generality directed along the coordinate axes. The two-dimensional intensity distribution $I_{ex}(x,y)$ is given by the absolute square of the amplitude $A_{ex}(x,y)$. The vector $[\Delta x, \Delta y]$ describes the spatial displacement of the pattern. The absolute spatial frequency k is for symmetry reasons assumed to be equal for four of the plane waves, depending on their simulated angle of incidence onto the focal plane, which in turn depends on the length of the unit cell in the pattern displayed on the SLM. The real-valued constant m (in Fig. 2a, $m = 1$) originates from the zero-diffraction order. As observable in Fig. 2a, the coherent superposition of the amplitude spread functions leads to bright 'ghost-spots' (grey arrow) at positions between the nominal imaged spot positions (four of them marked by white arrows). The removal of the zero diffraction order from the illumination simplifies the pattern (Fig. 2b), now having twice the spatial frequency of the nominal image periodicity.

$$A_{ex}(x,y) = \exp(ik(x - \Delta x)) + \exp(-ik(x - \Delta x))$$
$$+ \exp(ik(y - \Delta y)) + \exp(-ik(y - \Delta y)) \quad (2)$$

$$I_{ex}(x,y) = A_{ex}(x,y)A_{ex}^*(x,y)$$

Incoherent illumination from all accessible spatial directions to the grid would mostly remove the 'ghost spots' in Fig. 2a and would theoretically permit the transmission of a pattern up to twice the spatial frequency when compared to

the coherent perpendicular illumination case. Thus, the limit of high spatial frequency generation in the illumination pattern using coherent illumination suppressing the zero order is identical to incoherent illumination and a reduced unit cell in the SLM pattern. However, the coherent case leads to an optimised contrast in the object plane. A practical difficulty when illuminating with coherent light is the avoidance of the appearance of speckles.

In the following section the coherent situation with suppression of the zero diffraction order (Fig. 2b and c) is assumed. For the Fourier transformed intensity I_{ex} this results into 3×3 orders placed in a square reciprocal lattice, which is rotated by $45°$ (Fig. 2d).

2.2. Fluorescence saturation

Driving a large fraction of the fluorophore population into the singulet excited or the triplet state (fluorescence saturation) causes a non-linear dependence of the local fluorescence emission intensity on the illumination intensity. For the sake of simplicity this effect was simulated by

$$I_{em}(x, y) = Em(x, y)\rho(x, y)$$

$$Em(x, y) = \frac{fI_{ex}(x, y)}{f + I_{ex}(x, y)} \quad (3)$$

with $I_{ex}(x, y)$ representing the excitation intensity (with its maximum normalised to 1), $I_{em}(x, y)$ denoting the emission intensity (except for a constant factor which does not matter), which is proportional to the fluorophore density ρ and the spatially dependent emittability $Em(x, y)$. The characteristic saturation factor (f) for the simulations involving saturation was 1/5. Eq. (3) corresponds to a simple two-state model of fluorescence saturation (Sandison et al., 1995; Tsien and Waggoner, 1995; Heintzmann et al., 2002), with a relative saturation α (ratio of the emitted intensity to the maximal possible emission) of 5/6 at the strongest simulated excitation intensity.

Depending on the experimental conditions and selected fluorophores, some deviations from Eq. (3) may occur but are not expected to significantly perturb the general results.

Even under fluorescence saturation conditions, the intensity in every image is linearly related to the fluorophore density in the sample. For this reason the *emittability* $Em(x, y)$ has been introduced to characterize the spatially dependent ability of a fluorophore to emit light (Heintzmann et al., 2002). The emittability is calculated by application of Eq. (3) to the illuminating intensity pattern, omitting ρ. Fig. 2c displays an emittability obtained from the illumination intensity pattern of Fig. 2b.

2.3. Image formation

In Fig. 3 the object (Fig. 3a) is displayed along with images (no noise applied) simulated at two successive positions (phases) of the excitation spot raster as defined by
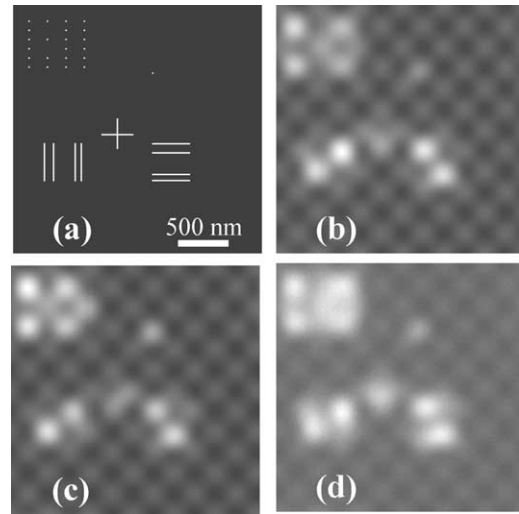

Fig. 3. The simulated object and its images at different excitation phases. (a) The object used in the simulations. For the sake of clarity, low intensities have been enhanced. (b) A simulated image assuming a linear relationship at the first position (phase) of the excitation pattern. (c) The simulated image at the second position of the excitation pattern. (d) Simulation of the non-linear saturation effect at the first excitation phase (compare with (b)).

Δx and Δy in Eqs. (1) and (2) (Fig. 3b and c). A noticeable difference in the detected intensity, depending on the position of the excitation pattern, is visible. In Fig. 3b and c, a linear dependence of the fluorescence emission on the excitation intensity was assumed, whereas in Fig. 3d, the saturation according to equation 3 was included. As expected, saturation leads to a decrease in contrast. To demonstrate that the SPEM method does not require the appearance of exact zeroes in the illumination pattern, a general intensity offset of 10% was added prior to saturation. This corresponds to a 90% modulation depth of the illumination pattern in the sample.

2.4. Image reconstruction

To understand the data reconstruction process of PEM or SPEM data, it is useful to investigate the data in Fourier-space during various steps of the reconstruction (Fig. 4). Widefield fluorescence imaging with flat illumination acts like a mask (Fig. 4b) on the Fourier-transformed object (Fig. 4a) by virtue of its multiplication with the optical transfer function (OTF) that decays to zero above a limiting frequency. Linear patterned excitation leads to a convolution of the object with the Fourier-transformed intensity distribution prior to the 'masking' imaging process. The object's zero spatial frequency is strongest. When illuminating with a pattern, this object zero frequency can be observed to appear at multiple positions (four out of the nine such places are marked by arrows) in the Fourier-transformed PEM image (Fig. 4c), indicating the presence of overlapping multiple shifted object components, which have to be separated for the reconstruction.
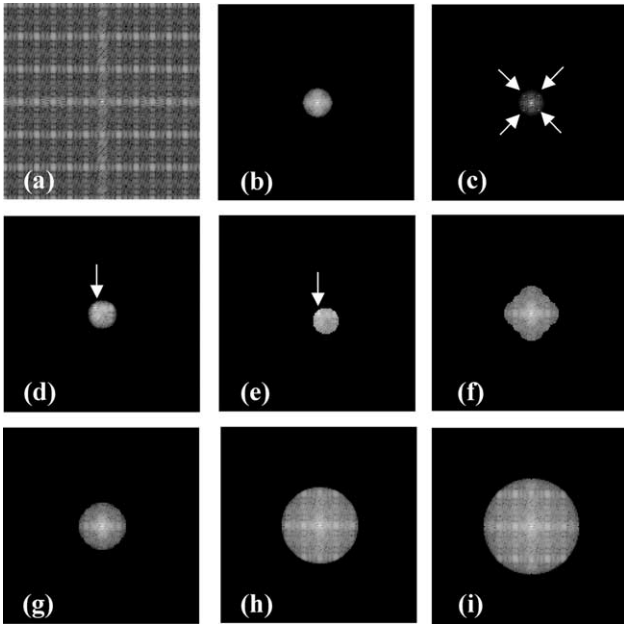
Fig. 4. Steps of the reconstruction in Fourier-space. In these simulations, no photon noise was applied and from panel (e) on the imaging OTF has been corrected. (a) Fourier-transformed object. (b) Simulated widefield image of the object. (c) A single image using linear patterned excitation (no saturation). (d) Extracted first order component. (e) This component shifted as to align the zero frequency with the object zero frequency (indicated by the arrow). (f) All 3×3 extracted components pieced together. No final apodization has been performed. (g) Apodization of (f) with a relative frequency of 0.25. (g) Magnitude in Fourier-space of a SPEM reconstruction (with saturation, 7×7 components, apodized to 0.4) (h) SPEM reconstruction (with saturation, 9×9 components, apodized to 0.5).

Imaging at various spatial positions of the excitation pattern permits such a separation. This is achieved by inverting an equation system that models the varying complex valued phase contribution of each object component to the measured image. The forward model can be approximated as

$$\tilde{I}_n(k_x, k_y) = \sum_l M_{\ln} \tilde{\rho}_l(k_x, k_y)$$

$$M_{\ln} = c'_l \exp\left(2\pi i \left(\frac{l_x n_x}{s_x} + \frac{l_y n_y}{s_y}\right)\right) \tag{4}$$

$$l_x \epsilon \{-m_x ... m_x\}, \qquad l_y \epsilon \{-m_y ... m_y\},$$

$$n_x = \{0...s_x - 1\}, \qquad n_y = \{0...s_y - 1\}$$

where l is an index iterating consecutively over each of the accounted two dimensional positions of the reciprocal grating (indexed by l_x and l_y) caused by the SLM, which is in this case assumed to be of rectangular shape accounting for $2m_x + 1$ positions along the k_x direction

and $2m_y + 1$ positions along k_y. The number n indexes (by n_x and n_y) the $s = s_x s_y$ images acquired at equidistant steps ($1/s_x$ of the unit cell along X and $1/s_y$ of the unit cell along Y) along the respective x and y spatial position. Eq. (4) has been constructed for the case of real space movements corresponding to the principal basis vectors in reciprocal space. In the simulated situation there is a 45° rotation between movement $[\Delta x, \Delta y]$ and the basis vectors of reciprocal space. This can however be incorporated by iterating $[n_x, n_y]$ over the set up phase shift vectors as expressed in the basis system of the reciprocal grid directions.

To solve the above equation system, the inverse (or pseudo-inverse) of the matrix $M_{\ln}$ can be applied to the vector defined by the Fourier-transformed (indicated by the tilde '~') measured images $\tilde{I}_n(k_x, k_y)$ yielding a vector of the individual object component values at each pixel $\tilde{\rho}_l(k_x, k_y)$. Due to the linearity of the Fourier-transformation, this step can actually be performed in real space. It should be noted, that the equation system can become singular under some conditions, which has to be avoided. The extracted object components $\tilde{\rho}_l(k_x, k_y)$ (Fig. 4d) can then be shifted by $[s_{x,l}, s_{y,l}]$ (Fig. 4e), such that the zero object frequency is at the origin of the reciprocal space. In the simulations presented here, the shift vector was calculated from the image data, as follows.

2.4.1. Automatic determination of the excitation pattern

For reconstruction, it is necessary to know the precise distances and positions of the excitation pattern. Although this can in theory be known a priori, it is often difficult to achieve in practice. An automatic determination of the grid spacing unit vectors of the excitation pattern (in this case along the diagonals), as well as the precise position of the grid in the first acquired frame is therefore highly desirable. This has been achieved by an approach based on cross-correlation (Gustafsson, 2000; Gustafsson et al., 2000). For order separation, previous knowledge of the grid spacings is not required. The separated components can then be used to determine the spacings. Since the position of the first order can at most slightly exceed the range of transferable spatial frequencies (due to the shorter excitation wavelength) its attached object component of first order will always have an overlap-region in Fourier-space with the information contained in the widefield-like zero order component. Since the information in the overlap region should be identical, the relative shift of the components in Fourier-space can be obtained by a precise determination (with sub-pixel accuracy) of the maximum of their cross-correlation function. This defines the real-space grid-spacing and thus the distances between all orders along this spatial direction. Sub-pixel accuracy was reached by the determination of the centre of mass of the magnitude of the cross-correlation function in a 3×3 pixel region around the maximum after subtraction of the minimum in this region:

$$p_x = i_{\max} + \frac{\sum\limits_{i,j=-1}^{1} i \left[\mathrm{CC}(i_{\max}+i, j_{\max}+j) - \min\limits_{i,j=-1}^{1} \mathrm{CC}(i_{\max}+i, j_{\max}+j) \right]}{\mathrm{Sum}}$$

$$p_y = j_{\max} + \frac{\sum\limits_{i,j=-1}^{1} j \left[\mathrm{CC}(i_{\max}+i, j_{\max}+j) - \min\limits_{i,j=-1}^{1} \mathrm{CC}(i_{\max}+i, j_{\max}+j) \right]}{\mathrm{Sum}} \qquad (5)$$

$$\mathrm{Sum} = \sum\limits_{i,j=-1}^{1} \left[\mathrm{CC}(i_{\max}+i, j_{\max}+j) - \min\limits_{i,j=-1}^{1} \mathrm{CC}(i_{\max}+i, j_{\max}+j) \right]$$

where $i_{\max}$ and $j_{\max}$ denote the x- and y-index respectively of the maximum pixel in the absolute magnitude of the two-dimensional cross-correlation function $\mathrm{CC}(i,j)$.

Through a similar shift determination for one perpendicular first order, the two dimensional grid-spacing and thus the relative shift of each extracted component could be determined. The relative grid position of the first image was determined by evaluating the complex phase of the zero frequency of the two respective back-shifted first order components. It should be noted that these positions can also be determined from the cross-correlation (Gustafsson, 2000; Gustafsson et al., 2000).

2.4.2. OTF compensation and weighted averaging

The effect of the widefield-like emission OTF $\tilde{h}_{\mathrm{em},i}(k_x + s_{x,i}, k_y + s_{y,i})$ on the extracted and shifted object components $\tilde{\rho}_i(k_x - s_{x,i}, k_y - s_{y,i})$ was compensated, and these extracted, compensated and shifted components were averaged, with weights depending on the pixel position in Fourier-space (Fig. 4f):

$$\tilde{I}_{\mathrm{rec}}(k_x, k_y) = \frac{\sum\limits_{i=1}^{(2m_x+1)(2m_y+1)} \frac{\alpha_i \tilde{\rho}_i(k_x - s_{x,i}, k_y - s_{y,i})}{(\sigma_i \alpha_i)^2}}{\sum\limits_{i=1}^{(2m_x+1)(2m_y+1)} \frac{1}{(\sigma_i \alpha_i)^2}},$$

$$\alpha_i = \frac{\tilde{h}_{\mathrm{goal}}(k_x, k_y)}{\tilde{h}_{\mathrm{em},i}(k_x + s_{x,i}, k_y + s_{y,i})} \qquad (6)$$

The σ_i denote the standard deviations of the noise levels, estimated from high spatial frequencies of $\tilde{\rho}_i(k_x, k_y)$, for which the signal level should be zero. The reconstructed Fourier-transformed image $\tilde{I}_{\mathrm{rec}}(k_x, k_y)$ was finally transformed back to real space.

Weighted averaging in Fourier-space is described in a second article in this journal (Heintzmann et al., 2003), where the method is applied to data obtained at different pinhole settings of a confocal microscope. This concept has been introduced in Gustafsson (2000). The method employed in the simulations presented here is identical to that in Heintzmann et al. (2003), in which assumptions for the relative strength of the components were required. In the data presented here, the relative strengths were obtained by analysing the Fourier-transform of the emittability pattern.

Some very small higher-order components were completely omitted. The scaling factors depend on the chosen illumination intensity as well as on the shape of the saturation curve. Thus a precise experimental characterization of a specific fluorophore is essential for its use in SPEM, especially if its behaviour deviates from the model given in Eq. (3). It should be noted that the relative strengths of the separated components may also be obtained by comparison of their relative magnitude (Gustafsson, 2000; Gustafsson et al., 2000).

The averaged components lead to a non-isotropic border-frequency in Fourier-space (Fig. 4f). In addition, the abrupt drop in spectral power in Fourier-space causes ring-shaped artefacts in real-space. To avoid both of these effects, a final apodization is applied to the reconstructed data (Fig. 4g). In the simulations with saturation (SPEM) the principle of reconstruction is identical to the non-saturated case except for the fact that many more components have to be separated and accounted for. In the cases presented here, these are $7 \times 7 = 49$ components (Fig. 4h) and $9 \times 9 = 81$ components (Fig. 4i). The goal function of the OTF after apodization was

$$\tilde{h}_{\mathrm{goal}}(k_x, k_y) = \begin{cases} (k_x^2 + k_y^2) < k_{\max}^2 : & \cos\left(\dfrac{\pi\sqrt{k_x^2 + k_y^2}}{2k_{\max}} \right) \\[3ex] (k_x^2 + k_y^2) \ge k_{\max}^2 : & 0 \end{cases} \qquad (7)$$

As noted in Heintzmann et al. (2003) based on Sementilli et al. (1993) and Gabor (1946) this minimizes the second moment of the PSF, projected along any in-plane direction. The apodization border $k_{\max}$ measured in relative frequency to the image border in Fourier-space (in X or Y) was selected as 0.25 (3×3 components), 0.4 (7×7 components) and 0.5 (9×9 components), yielding close to isotropic data for Fig. 4g–i.

3. Results

The real-space reconstructed results of the simulations are displayed in Fig. 5. In all of these simulations photon noise (10^4 photons at the maximum) was applied. This high amount of photons was necessary for the reduction of
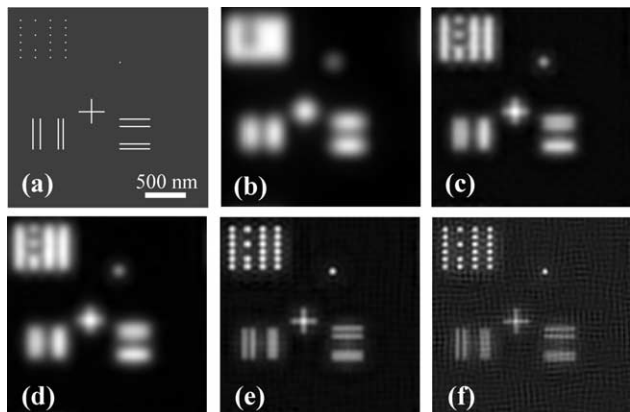
Fig. 5. Reconstruction of the object from the image data. (a) The object used in the simulations (clipped at high intensities to enhance the structure). (b) A calculated widefield image of the object. (c) Reconstructed image from 81 images without saturation (linear PEM case, corresponding to Fig. 4f). (d) Apodized PEM reconstruction to yield an isotropic resolution (corresponding to Fig. 4g). (e) Reconstruction from data including saturation (7×7 orders accounted for, with final apodization). (f) Reconstruction from SPEM data accounting for 9×9 orders including final apodization.

Fig. 7. Simulated point spread functions. No photon noise was applied in this simulation. The full width of half maximum for the curves was determined to amount to 215 nm (Widefield), 118 nm (Linear PEM), 70 nm (7×7 SPEM), 57 nm (9×9 SPEM) respectively.

artefacts in the SPEM-reconstruction using 9×9 components. In Fig. 5, a substantial increase in resolution is observed, depending on the number of components. However, it is also obvious that high-resolution images are influenced by noise to a higher degree, resulting in striped artefacts, which at the lower photon levels completely destroy the image structure (data not shown). Even in the noise-free case, residual artefacts can still be observed (Fig. 6a). These are assumed to originate from the higher orders introduced by the saturation process, which are not accounted for in the reconstruction.

These simulations were a worst-case situation. For a 9×9 components reconstruction assuming 100% modulation, no fluorescence background in the sample and a maximum of 10^3 photons per pixel, the resultant image quality was satisfactory (Fig. 6b).

A noise-free calculation was also performed and the full width at half maximum (FWHM) of the point-object evaluated by fitting a Gaussian distribution to the reconstruction results (Fig. 7). The increase in
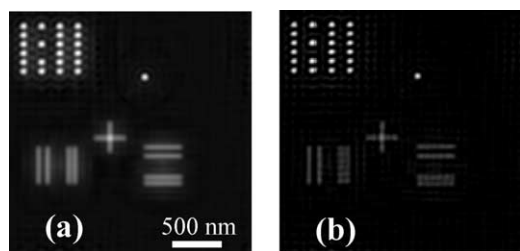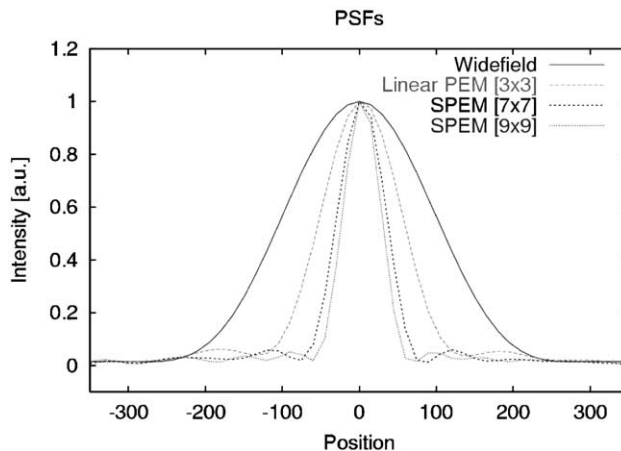
resolution depended on the number of orders considered in the reconstruction.

3.1. Required minimum number of images

An important issue is the minimum number of images required for successful reconstruction. At first glance, it seems that at least as many images (s) as total number of orders to separate [$m = (2m_x + 1)(2m_y + 1)$] are required. Re-evaluating the situation from the perspective of information theory (Cox and Sheppard, 1986), however, leads to a different view. Assuming n pixels in Fourier-space, which can in principle be determined in the final reconstruction and r pixels in Fourier-space being inside the detection OTF in each raw image, a number of $s \geq n/r$ images could be sufficient to yield an unambiguous result. However, the above consideration has to be viewed with care, since it presupposes a non-redundant situation in the raw data. In the current situation with at least m required images, some pixels in Fourier-space are determined multiple times and then averaged (by the weighted averaging approach). To reduce the number of required images, it should therefore be possible to dispose of multiple determination of Fourier-space pixels and instead include this redundancy into the equation system that connects the components. A single pixel of the measured raw data in Fourier-space is the sum of m overlapping orders. However, identifying the positions in Fourier-space to which the extracted components of this pixel contribute in the final reconstructed result (after shifting and reassembling), it can be seen that some of these positions remain within the range of the detection OTF (as an example the situation for 3×3 component PEM is shown in Fig. 8a). All of these connected pixels (seven connected pixels exemplified in Fig. 8a) have overlapping information content and it is thus useful to describe them in a single equation system. All of the reconstructed orders are placed on a regularly spaced reciprocal lattice (the order lattice)
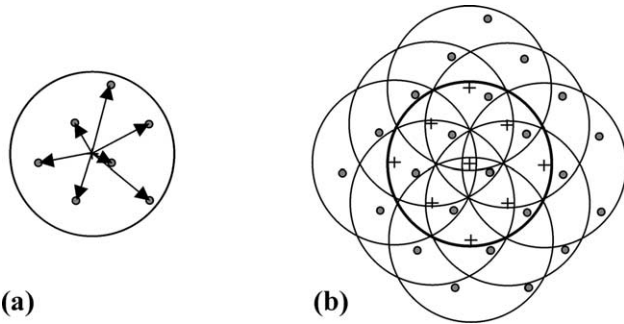

Fig. 6. Influence of photon noise. (a) If no photon noise was introduced this reconstruction was obtained assuming 9×9 components under saturation conditions. (b) In this simulation, only 1000 photons in the maximum pixel have been applied. However, no background fluorophore and 100% modulation degree were assumed. For better visualization, negative values were assigned to zero.

Fig. 8. Possible equation system for the 3 × 3 linear case accounting for the order information in 2D. (a) The Fourier-transformed range of raw-data modified by the OTF with its limit indicated by a circle. The gray spots indicate the positions that can be connected by a single equation system. The arrows indicate the *k*-vectors to these spots in the raw data. (b) The positions of the gray spots in the reconstructed Fourier-transformed data. Due to the symmetries of the emittability pattern, many spots overlap and only a total of 23 spots have to be determined. Four raw data images would thus be more than sufficient.

spanned by lattice unit vectors (Fig. 8b). Positions in the reconstructed Fourier-transform connected by integer combinations of order lattice vectors can be combined into a single equation system, avoiding the necessity for weighted averaging, but assuming the detection OTF is known a priori or determined from the experimental data. For the example pixels shown in Fig. 8a, seven independent measured data are acquired with every measurement. From this information a total of 23 regularly spaced pixels in the final reconstructed image (Fig. 8b) have to be determined. Thus 23 unknown reconstructed points need to be determined from s images, each containing the information for seven positions. It follows that $s = 4$ rather than $s = 9$ images are more than sufficient to determine the 23 unknown values in the nine reconstructed object components. However, the number of required images depends on the precise position of the points entered into the equation system. In the example shown in Fig. 8, a maximum number of images is required, when only four orders in the raw data are measured (Fig. 9). In this case
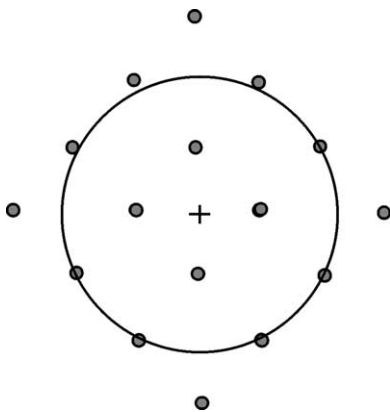

Fig. 9. Regions in the Fourier-transformed raw-data require a variable amount of images. In the worst case displayed here only four spots are present in the raw data with a total number of 16 spots to be determined, thus requiring four images of raw data.

16 positions are present in the reconstructed data, implying that four images are just about sufficient for this set of pixels. The required number of images is highly dependent on the distance between the zero and the first order. At larger lattice spacing this number increases, as would be expected from information theory.

4. Discussion

I have demonstrated in this work that 2D-patterned excitation is a suitable approach for linear and non-linear patterned excitation microscopy techniques. In the non-linear case, the practically achievable resolution depends on the signal-to-noise ratio (SNR) in the raw data, on the achievable degree of modulation and also on the relative contribution of background fluorescence that may also originate from out-of-focus light in a three-dimensional sample. In analogy to multi-point confocal microscopy, employing more sparsely distributed spots in the illumination pattern is expected to substantially reduce the influence of this out-of-focus fluorescence on the final reconstruction result, albeit at the expense of a larger number of components to account for and thus a large number of images to acquire.

An experimental realization of the simulated concept could, for example, be based on a Q-switched Nd:YAG laser with a pulse energy $> 10 \, \mu J$ per pulse, sufficient for saturating the fluorescence in a reasonable field of view. It is also possible to drive the system into triplet state saturation, depleting the ground state. A scheme for achieving resolution improvement base on ground-state depletion (GSD) has been suggested previously, albeit for a scanning approach (Hell and Kroug, 1995). Due to the much longer lived triplet-states light-sources such as pulsed flash-light systems could be used. Although Eq. (3) might not directly be applicable for GSD, a substantial non-linearity will arise and a good resolution enhancement can thus be expected.

The choice of the excitation pattern has a major influence on the reconstruction result. The higher order spots in the emittability distribution possessing only small strengths are the predominant cause for the noise in the reconstruction result. Shifting more spectral energy to these higher orders is therefore desirable.

At high numerical apertures, the vector nature of light can have a major impact on the strength of the illumination orders (private communications, M.G.L. Gustafsson). The polarization effects will reduce the interference contrast between most orders, a phenomenon that has not been accounted for in the presented simulations. At worst, two diffraction orders, each at an angle of 45° to the optic axis and parallel polarization will not interfere at all. Using a 1D-gridlike illumination and a polarization vector perpendicular to the optical plane of each refracted beam could have practical advantages, since this way permits the contrast to approach one, even in the high-NA case.

Furthermore, the choice of an illumination pattern of square-grid shape is far from spherically symmetric, causing a non-isotropic decay of the weights of the higher emittability orders.

An excitation pattern of three-fold symmetry (hexagonal) is expected to shift more energy into the high orders caused by saturation, as well as result in an advantageous more isotropic decay of orders. A hexagonal pattern with high contrast can be achieved by transmitting three orders near the border of the back-focal aperture with a relative angle of 120° if measured from the blocked zero order. An approximation to this situation can also be generated on a square grid.

From the simulations it is not yet clear whether a simultaneous or a successive application of differently shaped patterns (e.g. with different directions) leads to an optimal quality of the final image. Successive application of a series of different patterns can be realized via rotation of the excitation grid (Heintzmann and Cremer, 1999; Gustafsson, 2000) or by generating various patterns using a single programmable spatial light modulator (SLM). The SLM has practical advantages, since it does not require macroscopically movable parts and its programmability offers flexibility advantages (Hanley et al., 1999; Heintzmann et al., 2001).

It should be noted that the imaging OTF has to be known in order to generate a reconstruction. In the reduced equation system, connecting in the raw data different positions in reciprocal space, the system will depend on the exact position in reciprocal space under evaluation. In principle, the OTF could be used for correcting the raw data prior to application of the equation system, which reduces the problem to only a small fixed number of equation systems. However, in over-determined situations this could lead to sub-optimal results, since the relative strength of the information is not appropriately conserved.

The measured raw data, as well as the reconstructed data are real-valued, and thus the computation time and the required storage space can be reduced, since only half of the resulting Fourier-transformed image needs to be computed. For the equation system, however, this does not seem to lead to a reduction in the number of required images.

When a number of images greater than the number of required excitation phases is determined, the consideration presented above (Fig. 8) should lead to further improvement of the signal to noise ratio, since further constraints are placed on the data.

Considering the SPEM situation for 9×9 components (at a spot position similar to Fig. 9) the number of required images can be reduced quite substantially from 81 to 25 (4 spots per image, 10×10 spots for the reconstruction). In a similar manner, this approach can be applied to patterns of different symmetry or even to data taken successively with different patterning directions. It can also be extended in a straight-forward manner to a full 3D treatment of data stemming from three-dimensional samples.

A complication is that extreme care has to be taken when interpolations in Fourier-space are performed. Since the relative shift in Fourier-space can be a non-integer number of pixels along each spatial direction, the indicated vectors in the raw data do usually not align with the pixel positions. A possibility for circumventing this effect is to shift the raw data by the required amount though multiplication with $\exp(-ik\Delta x)$ in real space. The shifted raw data can then be used to determine the remaining values at the interpolated positions in Fourier-space. Fortunately these shifts (in this case 4) have to be performed only once since the geometry remains identical. The resulting final pixels still need to be shifted to their appropriate positions in Fourier-space. A disadvantage of this approach is that, for each pixel in Fourier-space, a different equation system has to be solved, potentially leading to long computation times. A further analysis of the properties of these equation systems will hopefully lead to a better understanding and thus result in a simplified solution. Simulations using this reduced equation system have not yet been performed, but a major improvement in signal-to-noise along with a reduction of required number of images is to be expected.

A reconstruction based on Maximum Likelihood (ML) is expected to further improve the results (Verveer and Jovin, 1997, 1998). ML-based reconstruction has the important advantage of correctly accounting for the properties of Poissonian photon statistics. Furthermore, it introduces constraints on the sample such as its positivity. This way, a reconstruction up to higher frequency regions (even beyond the measured frequency limit) is possible, simultaneously yielding a substantially improved signal to noise ratio. However, the results of ML-based methods depend on the sample structure, meaning that the result can no longer be described as a simple convolution of a resultant PSF with the object. An ML-based approach to the data treatment of patterned excitation data has, to my knowledge, not been developed to date.

Photobleaching possibly has an influence on the SPEM method. As discussed in Heintzmann et al. (2002), photobleaching will be more severe than in the linear methods only in cases where excited (singlet or triplet) state absorption plays a major role. It should also be noted that, although the simulations have been performed for the non-linear process of fluorescence saturation, a number of other coherent and non-coherent non-linear effects such as two-photon absorption, stimulated emission, Rabi-oscillations, coherent anti-stokes Raman scattering could possibly be employed in the same or at least very similar way.

In summary, two-dimensional patterned excitation offers practical advantages for linear as well as for non-linear cases. The SPEM simulations demonstrate the potential for exceptionally high resolution and there is a great potential to reduce the required number of images.

Acknowledgements

References

Egner, A., Hell, S.W., 1999. Equivalence of the Huygens–Fresnel and Debeye approach for the calculation of high aperture point-spread functions in the presence of refractive index mismatch. J. Microsc. 193, 244–249.

Cox, I.J., Sheppard, C.J.R., 1986. Information capacity and resolution in an optical system. J. Opt. Soc. Am. A 3, 1152–1158.

Frohn, J.T., Knapp, H.F., Stemmer, A., 2000. True optical resolution beyond the Rayleigh limit achieved by standing wave illumination. Proc. Natl. Acad. Sci. U.S.A. 97, 7232–7236.

Frohn, J.T., Knapp, H.F., Stemmer, A., 2001. Three-dimensional resolution enhancement in fluorescence microscopy by harmonic excitation. Opt. Lett. 26, 828–830.

Gabor, D., 1946. Theory of communication. J. Inst. Electr. Engng. 63, 429–457.

Gustafsson, M.G.L., 2000. Surpassing the lateral resolution limit by a factor of two using structured illumination microscopy. J. Microsc. 198, 82–87.

Gustafsson, M.G.L., Agard, D.A., Sedat, J.W., 2000. Doubling the lateral resolution of wide-field fluorescence microscopy using structured illumination microscopy. In: Conchello, J., Cogswell, C.J., Wilson, T. (Eds.), Three-dimensional and Multidimensional Microscopy: Image Acquisition and Processing VII, Proceedings of SPIE, vol. 3919, pp. 141–150.

Hanley, Q.S., Verveer, P.J., Gemkov, M.J., Arndt-Jovin, D., Jovin, T.M., 1999. An optical sectioning programmable array microscope implemented with a digital micromirror device. J. Microsc. 196, 317–331.

Heintzmann, R., Cremer, C., 1999. Laterally modulated excitation microscopy: improvement of resolution by using a diffraction grating. In: Bigio, I.J., Schneckenburger, H., Slavik, J., Svanberg, K., Viallet, P.M. (Eds.), Optical Biopsies and Microscopic Techniques III, Proceedings of SPIE, vol. 3568, pp. 185–196.

Heintzmann, R., Hanley, Q.S., Arndt-Jovin, D., Jovin, T.M., 2001. A dual path programmable array microscope (PAM): simultaneous acquisition of conjugate and non-conjugate images. J. Microsc. 204, 119–137.

Heintzmann, R., Jovin, T.M., Cremer, C., 2002. Saturated patterned excitation microscopy-a concept for optical resolution improvement. J. Opt. Soc. Am. A 19, 1599–1609.

Heintzmann, R., Sarafis, V., Munroe, P., Nailon, J., Hanley, Q.S., Jovin, T.M., 2003. Resolution enhancement by subtraction of confocal signals taken at different pinhole sizes. Micron, in press. PII: S0968-4328(03)00054-4.

Hell, S.W., Kroug, M., 1995. Ground-state depletion fluorescence microscopy, a concept for breaking the diffraction resolution limit. Appl. Phys. B 60, 495–497.

Klar, T.A., Jakobs, S., Dyba, M., Hell, S.W., 2000. Fluorescence microscopy with diffraction resolution barrier broken by stimulated emission. Proc. Natl. Acad. Sci. U.S.A. 97, 8206–8210.

Sandison, D.R., Williams, R.M., Wells, K.S., Strickler, J., Webb, W.W., 1995. Quantitative fluorescence confocal laser scanning microscopy (CLSM). In: Pawley, J.B., (Ed.), Handbook of Biological Confocal Microscopy, 2nd ed, Plenum Press, New York, pp. 267–268.

Sementilli, P.J., Hunt, B.R., Nadar, M.S., 1993. Analysis of the limit of superresolution in incoherent imaging. J. Opt. Soc. Am. A 10, 2265–2276.

Schönle, A., Hänninen, P.E., Hell, S.W., 1999. Nonlinear fluorescence through intermolecular energy transfer and resolution increase in fluorescence microscopy. Ann. Phys. (Leipzig) 8, 115–133.

Tsien, R.Y., Waggoner, A., 1995. Fluorophores for confocal microscopy. In: Pawley, J.B., (Ed.), Handbook of Biological Confocal Microscopy, 2nd ed, Plenum Press, New York, pp. 260–272.

Verveer, P.J., Jovin, T.M., 1997. Efficient superesolution restoration algorithms using maximum a Posteriori estimations with application to fluorescence microscopy. J. Opt. Soc. Am. A 14, 1696–1706.

Verveer, P.J., Jovin, T.M., 1998. Image restoration based on Good's roughness penalty with application to fluorescence microscopy. J. Opt. Soc. Am. A 15, 1077–1083.